AIAA JOURNAL
Vol. 56, No. 9, September 2018

Technique for Enhanced Flow Control Efficiency Through Thermal Actuation

Damian Hirsch*
California Institute of Technology, Pasadena, California 91125
Arvin Shmilovich†
The Boeing Company, Huntington Beach, California 92647
Edward Whalen‡
The Boeing Company, Hazelwood, Missouri 63042
and
Morteza Gharib§
California Institute of Technology, Pasadena, California 91125

DOI: 10.2514/1.J056944

Thermal active flow control has been developed to enhance the efficiency of active flow control systems. The actuation concept is derived from gas-dynamics principles, and it is based on thermal control of the air supply. It is shown that higher air supply temperatures result in reduced mass flow rate with no degradation in active flow control performance. A computational method has been used to systematically investigate the hot air supply approach for isolated blowing actuators and fluidic oscillators. Subsequently, the thermal control concept has been computationally evaluated for airplane applications. These include enhanced control authority of a vertical tail and an airplane high-lift system, confirming the trends observed from the gas-dynamics analysis with regard to reduced actuation input as a function of supply temperature. Further confirmation of the thermal actuation concept was experimentally obtained for a bench-top actuator and a vertical-tail model in a wind-tunnel setting. The paper introduces potential approaches for system integration associated with heated supply, while highlighting the benefit of using available high-temperature sources for active flow control.

Nomenclature

A	=	cross-sectional area of nozzle, m^2
A_{ref}	=	aerodynamic reference area, m^2
a	=	sonic speed, m/s
C_μ	=	momentum coefficient, $\dot{m}u_{\text{jet}}/((1/2)\rho_\infty u_\infty^2 A_{\text{ref}})$
C_L	=	lift coefficient
C_p	=	pressure coefficient
C_Q	=	mass flow coefficient, $\rho uA/(\rho_\infty u_\infty A_{\text{ref}})$
C_Y	=	side-force coefficient
M	=	Mach number
$\dot{m}$	=	mass flow rate, kg/s
PR	=	pressure ratio, p_{0_1}/p_{0_∞}
PT	=	normalized total pressure
p	=	pressure, Pa
$\bar{q}$	=	velocity magnitude, m/s
R	=	specific gas constant, J/(kg · K)
T	=	temperature, K
TR	=	temperature ratio, T_{0_1}/T_{0_∞}
u	=	velocity, m/s
γ	=	heat capacity ratio
ρ	=	density, kg/m^3

Subscripts

ex	=	exit
in	=	inlet
th	=	throat
0	=	stagnation
∞	=	freestream

Superscript

$'$	=	normalized

I. Introduction

ACTIVE flow control (AFC) is an emerging technology that aims at enhancing the performance of flight vehicles. The effectiveness of AFC has been demonstrated in numerous aerodynamic and propulsion applications with various types of AFC devices [1]. The most widely used control systems can be classified into two groups. One class consists of piezoelectric actuators, which generate pulsed suction/blowing flows, sometimes referred to as zero-net-mass-flux or synthetic jets. Examples of studies using piezoelectric actuation for separation control are described in Refs. [2–6]. The main advantage of these actuators is that they are electrically powered. However, their major limitation is their inability to produce jets with high enough momentum for full-scale problems of engineering interest. The other group consists of fluidic actuators, which are capable of overcoming this limitation, but they require a supply of compressed air. These devices aim to introduce flow perturbations in various forms using a variety of actuators: constant blowing actuators [7–9], pulsed blowing devices [10–14], fluidic oscillators [15–18], sprinkler systems [10,12,19–21], and traversing jet actuators [9,22]. An interesting offshoot of the pulsed blowing family is the combustion-based actuator, which produces pulsed high-temperature high-pressure jets [23,24]. The prospective use of the AFC technology using fluidic actuators has become particularly relevant after a series of experimental evaluation [15,17,25] and the successful demonstration of a full-scale AFC system in flight [26] on the Boeing 757 ecoDemonstrator.

Presented as Paper 2017-3040 at the 35th AIAA Applied Aerodynamics Conference, Denver, CO, 5–9 June 2017; received 14 November 2017; revision received 6 April 2018; accepted for publication 21 April 2018; published online 10 August 2018.

*Postdoctoral Scholar, Graduate Aerospace Laboratories, 1200 E California Blvd, MC 105-50.
†Technical Fellow, Boeing Research and Technology, 14900 Bolsa Chica Rd, H017-D335. Senior Member AIAA.
‡Flow Control Actuators Manager, Boeing Research and Technology, 325 James S. McDonnell Blvd, S306-4030. Senior Member AIAA.
§Director of GALCIT, Graduate Aerospace Laboratories, 1200 E California Blvd MC 105-50. Senior Member AIAA.

That research was performed under a collaborative project between NASA and the Boeing Company, with participation from the California Institute of Technology and the University of Arizona.

AFC based on fluidic actuators is especially effective, but they require air supply such as bleed air off an engine, an auxiliary power unit (APU), or a special-purpose compressor. The higher the AFC performance target (e.g., airplane incremental lift), the higher the input fluidic requirement (mass flow rate) is. A viable AFC system must consider the limited resources available onboard for attaining performance goals. Therefore, the key requirement for a successful and practical design is use of very low-mass flow input to achieve design targets. The purpose of this study is to enhance the efficiency of fluidic actuators by developing an actuation technique that requires low amount of air supply (referred to as low-input actuation throughout this paper).

The new actuation control is the knob that enables dialing down input to acceptable levels. It is based on thermal control of the air supply. Specifically, a higher air supply temperature results in reduced mass flow rate. Generally, the aerodynamic benefit from AFC is a function of the momentum coefficient due to actuation. Because the momentum coefficient is not dependent on temperature, the net impact of increased supply temperature results in reduced mass flow with no degradation in AFC performance. The thermal control introduces a new element in the system integration of AFC. Depending on the application, there are several approaches that might be considered for practical implementations.

In this paper, the thermal AFC concept is described through the application of gas-dynamics principles. This will be followed by computational confirmations for a family of steady blowing devices as well as fluidic oscillators. The efficiency of thermal actuation for separation control is demonstrated in airplane applications. These include the vertical-tail application for enhanced lateral control authority and flow control for improved performance during high-lift operation. The results of experimental studies will also be presented, further validating the thermal actuation concept. The experiments include a bench-top of a steady blowing actuator and a wind-tunnel test on a vertical tail employing an array of fluidic oscillators. The paper concludes with an overview of optional design strategies, while highlighting the benefit of using available high-temperature sources for AFC.

II. Thermal Flow Control Concept

The thermal actuation concept was first introduced in Shmilovich and Whalen [27], starting off with the characterization of the fluidic actuator. This was accomplished with a gas-dynamics approach to account for compressibility, and it ensures proper characterization across the pressure ratio range. First, the actuation parameters are expressed in terms of the pressure p and temperature T. For the one-dimensional flow of a compressible gas with velocity u at a section having an area A, the mass flow rate $\dot{m}$ and the momentum $\dot{m}u$ are

$$\dot{m} = \rho u A = \frac{\sqrt{\gamma} p}{\sqrt{RT}} MA \sim \frac{p}{\sqrt{T}} M \tag{1}$$

$$\dot{m}u = \rho u^2 A = \gamma p M^2 A \sim p M^2 \tag{2}$$

where ρ is the density, and M is the Mach number. Assuming an ideal gas with equation of state $p = \rho RT$ and speed of sound $a = \sqrt{\gamma RT}$, the mass flow rate and momentum are both functions of the pressure and the Mach number. Notably, however, the mass flow rate is proportional to $T^{-1/2}$, whereas the momentum is independent of the temperature. Because the flow control effect is generally a function of the momentum, the net impact of increased supply temperature is reduced mass flow, with no degradation in flow control performance. This temperature relationship forms the basis for the development of a more efficient actuation method using high-temperature supply.

Consider now the one-dimensional inviscid flow in a convergent–divergent nozzle. The supply is provided from a plenum having stagnation pressure and temperature of p_{0_j} and T_{0_j}, respectively. For a nozzle with a given cross-sectional area distribution, the Mach number M can be calculated at a station having an area A. Here, we consider a nozzle with an inlet area A_{in}, a throat area A_{th}, and nozzle exit area A_{ex}. The nozzle flow is discharged into an ambient flow that is parallel to the nozzle axis, with freestream Mach number M_∞ and stagnation properties of p_{0_∞} and T_{0_∞}. In the context of flow control, it is customary to express the mass flow rate and momentum as

$$C_Q = \frac{p_{0_j}}{p_{0_\infty}} \cdot \sqrt{\frac{T_{0_\infty}}{T_{0_j}}} \cdot \frac{M}{M_\infty} \cdot \frac{A}{A_{\text{ref}}} \cdot \left(\frac{1 + ((\gamma-1)/2)M^2}{1 + ((\gamma-1)/2)M_\infty^2} \right)^{-((\gamma+1)/2(\gamma-1))} \tag{3}$$

$$C_\mu = 2 \cdot \frac{p_{0_j}}{p_{0_\infty}} \cdot \left(\frac{M}{M_\infty} \right)^2 \cdot \frac{A}{A_{\text{ref}}} \cdot \left(\frac{1 + ((\gamma-1)/2)M^2}{1 + ((\gamma-1)/2)M_\infty^2} \right)^{-(\gamma/(\gamma-1))} \tag{4}$$

Here, the coefficients are referenced to the freestream conditions. The actuation input is prescribed by the total pressure and temperature ratios, $\text{PR} = p_{0_j}/p_{0_\infty}$ and $\text{TR} = T_{0_j}/T_{0_\infty}$. In functional form, the coefficients can be expressed as,

$$C_Q = f\left\{ \frac{p_{0_j}}{p_{0_\infty}}, \frac{M}{M_\infty}, \sqrt{\frac{T_{0_\infty}}{T_{0_j}}} \right\} \tag{5}$$

$$C_\mu = f\left\{ \frac{p_{0_j}}{p_{0_\infty}}, \left(\frac{M}{M_\infty} \right)^2 \right\} \tag{6}$$

Next, an analysis of the nozzle flow for a representative actuator geometry with an area ratio of $A_{\text{th}}/A_{\text{in}} = 0.4$ ($A_{\text{in}} = 0.05$, $A_{\text{th}} = 0.02$) is performed. The pressure and temperature at the inlet station are used to compute the flow properties at the throat where the momentum coefficient is commonly defined. The mass flow coefficient is also computed at the throat, although it is constant along the nozzle. The flow characteristics are presented in Fig. 1 for a set of flow scenarios over the range of practical pressure ratios. Plots of the mass flow and momentum coefficients at the throat station are shown as functions of the supply pressure ratio. Also shown are the C_μ versus C_Q plots. It is noted that any one of the flow cases shows two distinct segments. The lower ends of the lines represent subsonic conditions, where increased pressure results in increased velocity at the throat, leading to a sharp rise in C_μ. Once the actuator is choked, the throat velocity remains constant (for a given temperature). As the pressure further increases, the density increases linearly (because the inlet temperature is constant), and C_μ and C_Q exhibit a linear behavior.

The black curves represent the baseline nozzle flow for a range of pressure ratios and $\text{TR} = 1$. Point A represents an actuation obtained with a supply of $\text{PR} = \text{PR}_1$. As an example, assume that this condition achieves the targeted C_μ, but the mass flow rate needed is higher than the allowable amount $C_{Q_{\text{lim}}}$. One way to limit the mass flow rate is by reducing the throat area of the nozzle to $A_{\text{th}} = 0.02/\sqrt{2}$, shown by the blue lines. However, this is not satisfactory because it results in a lower C_μ (point B). The solution is provided by increasing the supply temperature to $\text{TR} = 2$, which is represented by the red curves (with the baseline nozzle, $A_{\text{th}} = 0.02$). In particular, point C is the condition achieved with $\text{PR} = \text{PR}_1$, where the C_μ target is attained using a reduced mass flow rate of $C_Q = C_{Q_{\text{lim}}}$. This nozzle flow analysis underscores the concept of thermal control for enhanced efficiency of AFC.

In the example illustrated previously, the objective is to lower the required mass flow rate without impacting actuator output. An alternative AFC design objective might call for higher actuator output for a certain amount of air supply. This problem can also be solved with thermal control. Starting with the reference condition A, we seek to increase momentum using $C_Q = C_{Q_A}$. This can be achieved by a combination of high-temperature and high-pressure supply. Referring to the C_μ versus C_Q plot in Fig. 1, an increase in temperature corresponds to point C, and increased pressure helps climb the red line branch until higher C_μ is achieved at C_{Q_A}. These examples illustrate that thermal AFC can be used to lower the amount

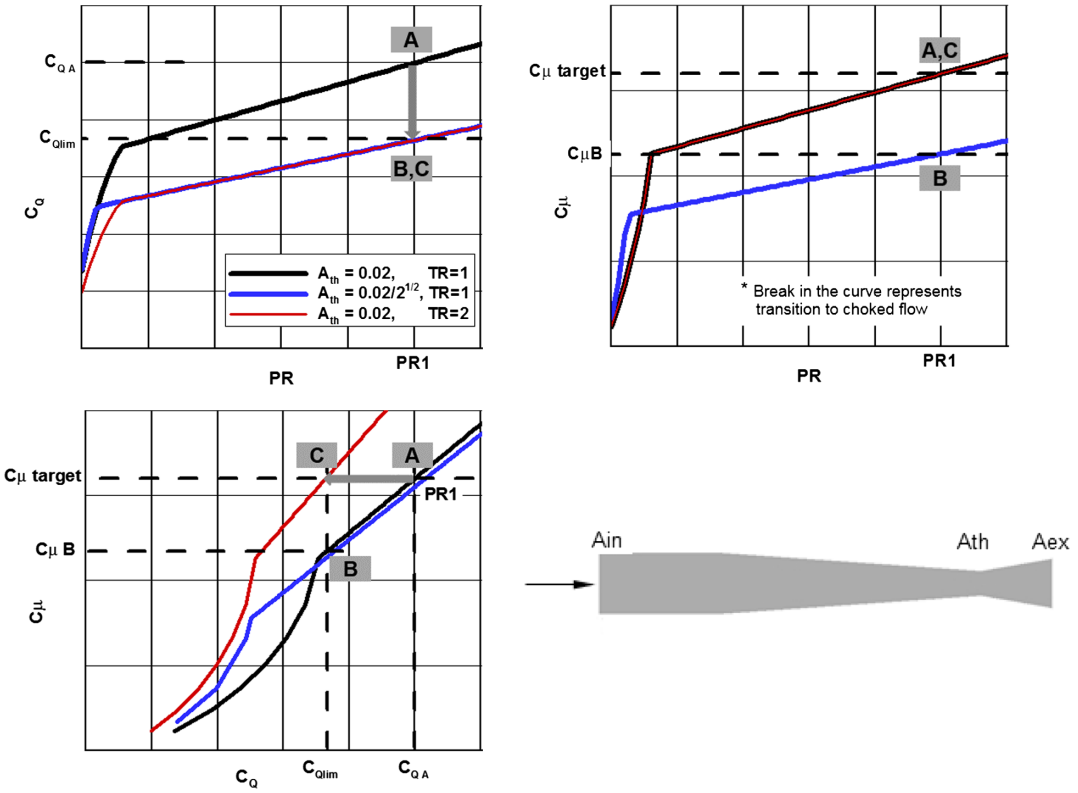

Fig. 1 Nozzle flow characteristics.

of mass flow rate, with no impact on actuator effectiveness, or to attain higher effectiveness for the same input level.

III. Numerical Procedure

The computational tool used for the simulations of thermal AFC is a modified version of the OVERFLOW code originally developed by NASA [28], and it forms the core process of Boeing's transport aircraft computational fluid dynamics. OVERFLOW is based on the unsteady Reynolds-averaged Navier–Stokes (RANS) formulation for overset grid systems. The numerical procedure has been modified to simulate flows for a family of flow control techniques [10,12,19–22,29,30]. In this study, the second-order Roe upwind-differencing scheme is used with the ARC3D diagonalized Beam–Warming scalar pentadiagonal scheme on the right-hand side. The Spalart–Allmaras turbulence model has proven robust in the context of flow control and is used for the simulation cases presented here. The time-stepping scheme is second-order, as demonstrated in the framework of AFC using a system with multiple actuators [31]. The numerical procedure has been extensively validated for numerous applications using various flow control methods [12,18,29,31,32]. The validation studies include the characterization of flow control devices for the range of practical actuation parameters as well as the performance of airplanes equipped with large systems of actuators.

IV. Computational Assessment of Isolated Actuators

The thermal AFC method has been applied to a family of actuators. Flow diagnostics is used to demonstrate the effect of the supply temperature on the required mass flow rate for actuation.

A. Fluidic Oscillator

The fluidic oscillator investigated in Refs. [15,33] and extensively validated with OVERFLOW in Ref. [18] is used for assessing the thermal control method. It consists of a symmetrical internal loop structure, so that, when subjected to high-pressure supply, it results in an unsteady feedback mechanism. This effectively produces a swiveling jet at the exit station, which influences the ambient flow over a large region. The actuator used for the simulations has a nonsymmetrical divergent segment (relative to the horizontal midplane of the actuator), where the top wall is shorter, as indicated in Fig. 2.

Figure 3 shows the computed flow characteristics in the fluidic oscillator with an air supply of PR = 4. A wide range of temperature levels, TR = 1, 2, and 4, is used to illustrate the range of applicability of the thermal heating approach. The time-averaged mass flux ρu (a measure of mass flow rate), momentum flux ρu^2, and temperature are shown at the inlet station, on a horizontal cut through the center of the actuator, and at a cross section just downstream of the exit station. The time-averaged flows are nearly symmetrical with respect to the actuator centerline, and they illustrate the broad area coverage of the ejection jets. For this high PR case at TR = 1, the average velocity and momentum profiles attain maximum values at the centerline. High velocity develops in the diffuser, resulting in lower tendency of the flow to attach to the diffuser walls and thereby diminishing the Coanda effect [18]. At the prescribed input pressure ratio, the actuator is chocked, and a highly unsteady system of shocks and expansion waves forms in response to the pressure differential along the diffuser. The oscillation frequency is 236 Hz. The black contour lines

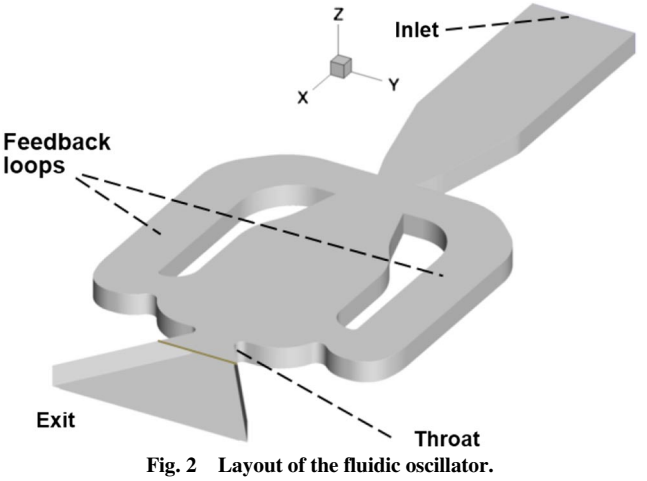

Fig. 2 Layout of the fluidic oscillator.

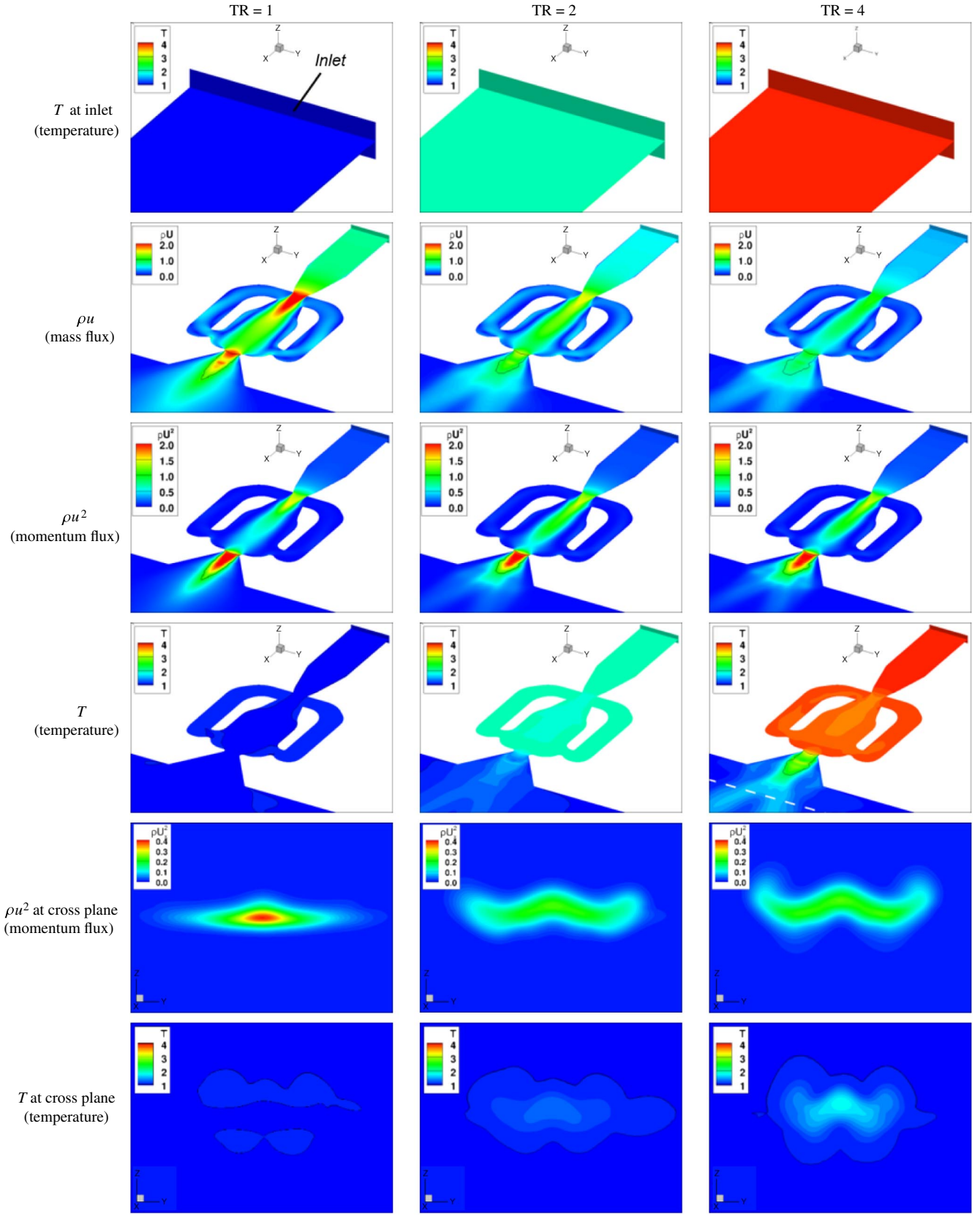

Fig. 3 Time-averaged effect of hot air supply on the flow of a fluidic oscillator (sweeping jet actuator). PR = 4 and varying TR are applied on the whole inlet section.

represent sonic conditions in the perspective views of ρu, ρu^2, and T. The black lines in the cross planes of the temperature plots signify the ambient condition $T = T_\infty$. The flowfields of the high-temperature cases are compared to the baseline case of cold air supply for which TR = 1. The computed flowfields show the formation of pockets of high velocity at the narrow passages at the intersection with the feedback channels and at the throat. This is particularly evident in the case of the cold supply.

For the hot air supply cases, the results indicate that ρu decreases when the inlet flow is heated up, whereas ρu^2 is invariant to the

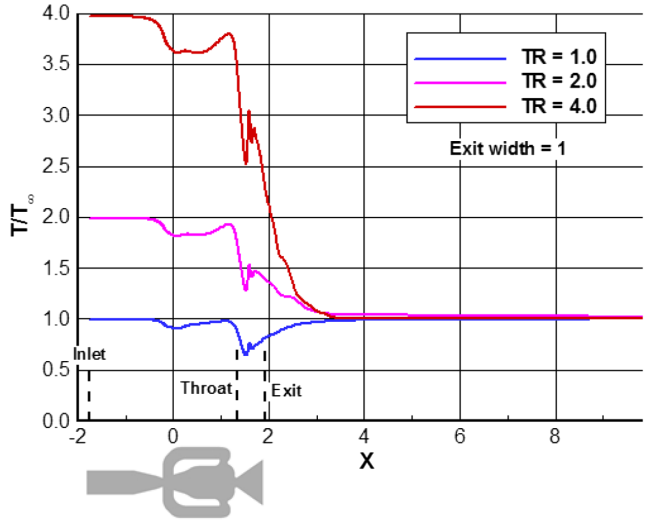

Fig. 4 Time-averaged temperature profiles along the actuator centerline. Inlet condition of PR = 4 with various TR.

temperature. The decrease in ρu increases the propensity of the flow to attach to the diffuser walls, thus amplifying the Coanda effect. This is evident from the double lopsided distribution, with pockets of relatively higher mass flux at angles of about 15 deg to the centerline. Likewise, in the cold-temperature case, where the flapping motion is reduced, the time-averaged momentum flux extends over a longer axial distance. However, the oscillation frequencies obtained with the higher temperatures are nearly identical to the cold air supply. As predicted from the gas-dynamics analysis, the mass flow rate is reduced by $1/\sqrt{\text{TR}}$, or 29% and 50% for the TR = 2 and TR = 4 cases, respectively. In the hot supply cases, the temperature is elevated up to the throat region. Interestingly, the temperature decays rapidly downstream of the throat section as the flow recompresses to the ambient condition. This implies that, even if very hot air supply is desired for major reduction in mass flow rate, the temperatures in the region where the actuators would be mounted will be much lower than the supply temperature, and it will be confined to a very small area. This point is also illustrated in Fig. 4, which shows the time-averaged temperature profiles along the centerline of the actuator.

The performance of fluidic oscillators with hot air supply is summarized in Fig. 5. The whole inlet hot supply shows a reduction in mass flow rate as a function of $1/\sqrt{\text{TR}}$ with no degradation in momentum. The cases that form the PR = 4 curves correspond to those in Figs. 3 and 4.

B. Constant Blowing Actuators

In certain applications, the constant blowing actuator is very effective. This device consists of a convergent–divergent nozzle with a rectangular cross section, as shown in Fig. 6. It is derived from the fluidic oscillator described in the previous section where the feedback loops are removed. The inlet, throat, and exit areas of

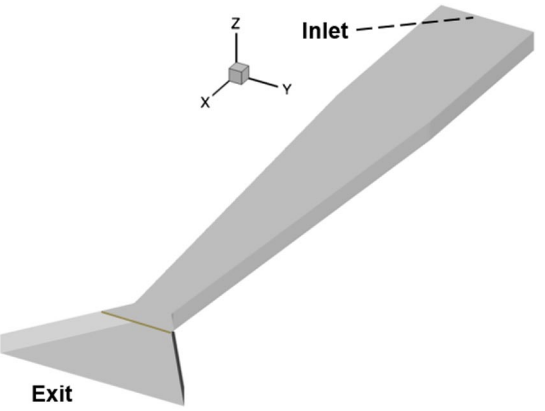

Fig. 6 Layout of the constant blowing actuator.

the blowing nozzle are identical to those of the fluidic oscillator. The effectiveness of the constant blowing nozzle in conjunction with thermal AFC is illustrated in Figs. 7 and 8 for PR = 4. The hot air supply is provided uniformly on the entire inlet section. Generally, the flow characteristics are similar to those of the fluidic oscillator in Figs. 3 and 4.

V. Computational Airplane Applications

The analysis described in the previous section illustrates that hot air supply helps reduce actuation mass flow rate with almost no impact on the momentum. In this section, the impact of the high-temperature supply on the flow is evaluated. Two implementations are considered using different forms of actuation.

A. Vertical Tail

Flow control has been recently applied to the vertical tail for enhanced airplane directional control [26]. The flow control technology was flight tested on the Boeing 757 ecoDemonstrator in 2015 in partnership with NASA to address a key goal of the Environmentally Responsible Aviation (ERA) Project in terms of reduced fuel consumption and lower emissions. The AFC system was powered by the compressed air generated by the airplane's auxiliary power unit (APU). Whether using an APU or other fluidic sources, a key objective for a future practical flow control system is use of low air supply. This is especially critical in applications where the enhanced performance sought from AFC is substantial. The thermal AFC provides the solution for lowering the mass flow rate required for effective actuation.

The full-scale model tested at the Arnold Engineering Development Complex National Full-Scale Aerodynamics Complex (NFAC) [17,25] before the AFC flight demonstration was used to establish the effectiveness of thermal actuation. Figure 9a shows the model mounted on an elongated blister representing the upper side of the fuselage at the airplane tail section. The analysis was performed for a rudder deflected at 30 deg, representative of a realistic flight

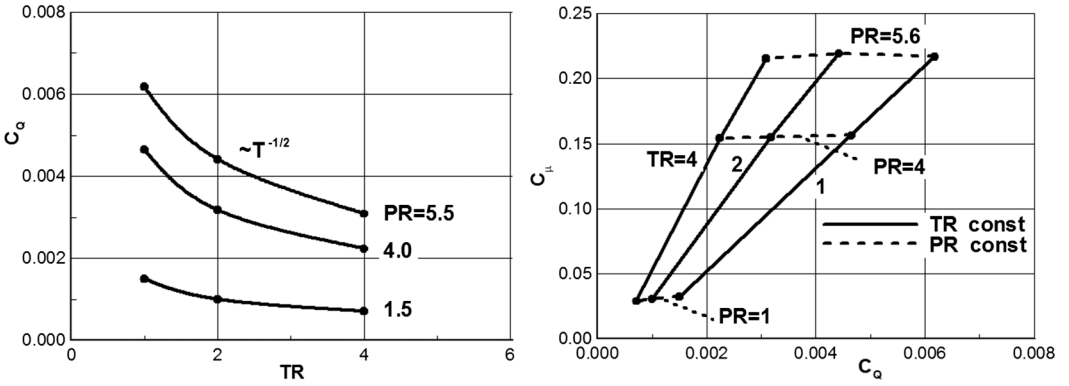

Fig. 5 Performance of fluidic oscillators with thermal AFC.

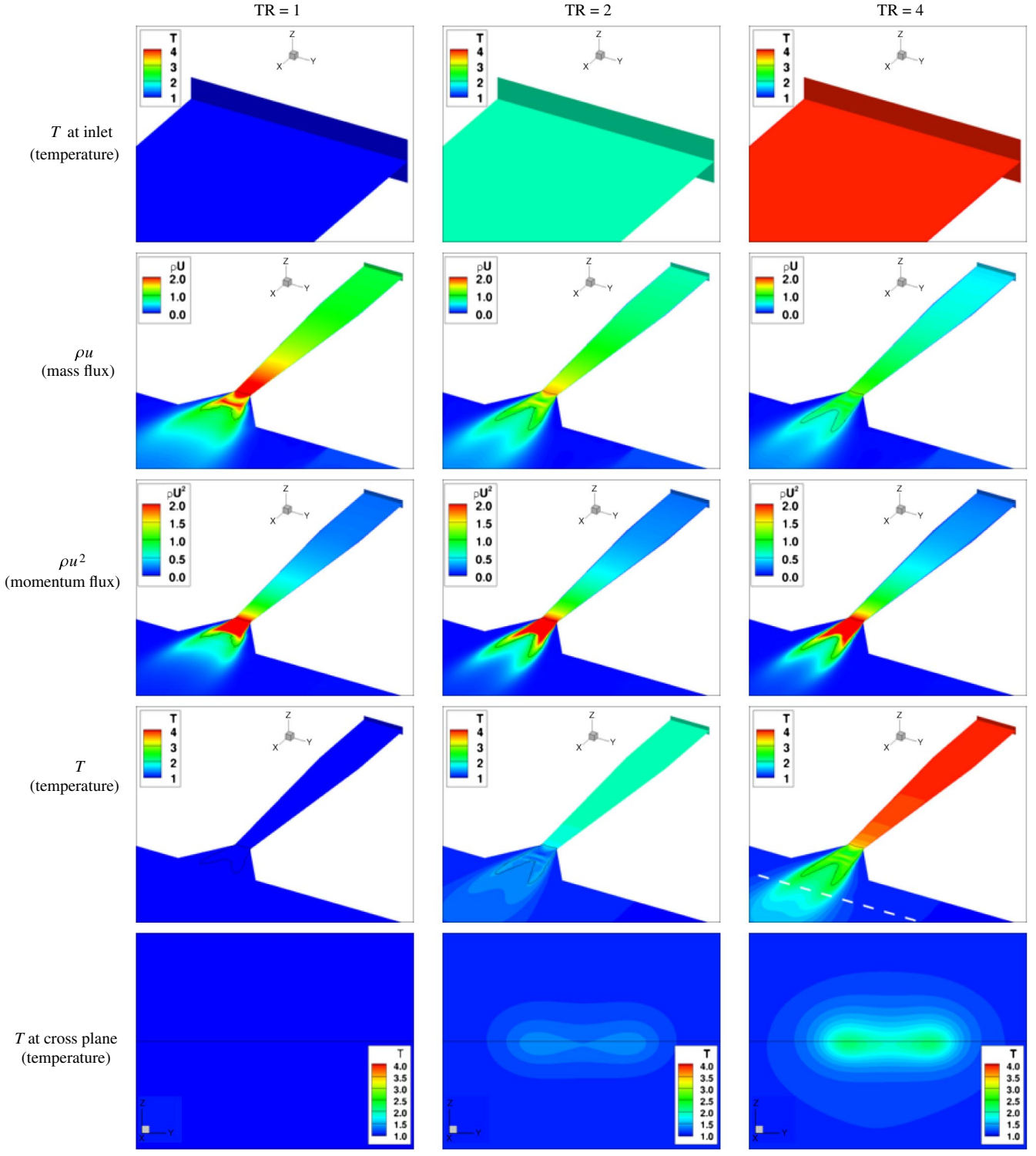

Fig. 7 Effect of hot air supply on a constant blowing actuator. Inlet condition of PR = 4 with various TR.

condition. The actuators are installed on the suction side of the tail (i.e., on the side opposite to the rudder deflection). The actuators' geometry was similar to the fluidic oscillator described in Fig. 2. A set of 37 actuators are embedded at the trailing edge of the stabilizer. This effectively placed the orifices of the actuators tangent to the rudder surface when it was being deflected. The centerlines of the actuators were perpendicular to the rudder hinge line. A close-up view of the actuators through the transparent tail surface is also shown in Fig. 9a. The actuators were placed at equal intervals along the tail, from a station close to its root to a section near the tip.

The computational model of the NFAC test includes the wind-tunnel walls. The upstream inflow boundary is chosen to mimic the state of the viscous flow at the model station in the absence of the model. The computational domain consists of overlapping grid systems that conform to all the solid surfaces, including the actuators. A set of fine subgrids are used for each orifice to resolve the interaction of the swiveling jets with the surrounding flow. The grid contains about 120 million points and 460 subgrids. Details of the computational setup can be found in Shmilovich et al. [18].

The solutions are obtained for zero sideslip and a freestream velocity of 51 m/s, which corresponds to a Mach number of 0.15. The Reynolds number is 17.5 million based on the mean aerodynamic chord of the vertical tail.

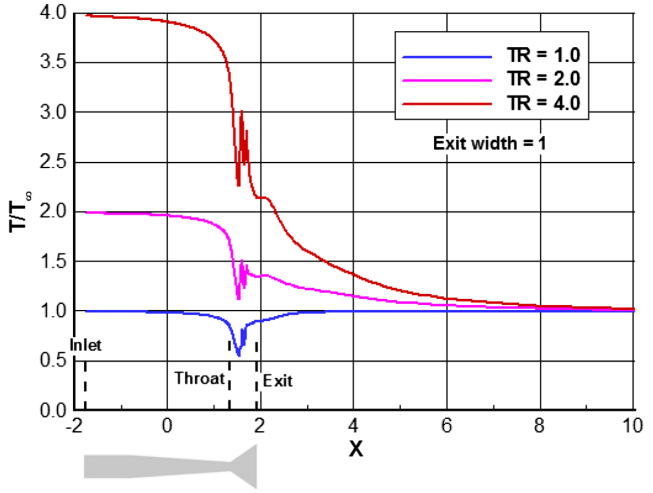

Fig. 8 Temperature profiles for a constant blowing actuator. Inlet condition of PR = 4 with various TR.

In the first step of the analysis, the baseline flow without actuation is obtained using a steady-state computation. The time-varying flowfields are then obtained for the actuated flows. Figure 9b shows the surface pressure distributions on the suction side of the tail, the blister element, and a portion of the mounting floor surrounding it. The flowfields include the flow separation bubbles (in gray surfaces) and the normalized total pressure PT at a cross-sectional cut just downstream of the tail assembly. At these conditions, the baseline flowfield (AFC off) is partly separated in the outboard segment, triggered by the adverse pressure gradient close to the hinge line. No separation occurs inboard due to the edge effect, which is a result of the flow through the gap created by the deflected rudder and the mounting blister. Also, a small pocket of flow separation forms at the leading edge of the blister. The cross-sectional cut depicts the wake profile, which consists of the tail wake element and the bounded viscous layer at the side of the mounting wall.

The effect of flow control applied at the inboard set of 31 actuators (of the array of 37 actuators) with PR = 3.2 and TR = 1 is also presented in Fig. 9b. The computed flowfield indicates that, in a time-average sense, the momentum imparted by the actuation generally provides more efficient flow turning along the rudder, which results in increased global circulation and higher side force. The actuation results in the elimination of flow separation on nearly the entire span, although remnants of flow separation bubbles exist close to the tip. The trailing-wake profile indicates that the viscous wake is mitigated due to actuation. The tip vortex gets stronger, commensurate with the increased tail loading and the sharper span load distribution. Figure 9c shows the Mach number contours on a cut through the actuators. At this high pressure ratio, the actuators are choked, and instantaneous Mach numbers of up to 1.7 are achieved.

The next set of results is obtained for PR = 3.2 and a set of temperature ratios, TR = 1.5, 2, and 4. The flowfields in Fig. 9d indicate that the actuation with higher temperature is just as effective, with flow features nearly identical to the cold-case actuation. The temperature fields in Fig. 9e show localized elevated temperatures in the immediate vicinity of the actuators. Note the zoomed-in scale in the inset of the TR = 1.5 case. The performance of the AFC system is shown in Fig. 10. The impact of the thermal AFC technique on the side force while reducing air supply illustrates that the thermal actuation provides a pathway toward higher efficiencies of large AFC systems. Relative to cold air supply, thermal actuation at TR = 4 reduces the mass flow rate by about 50%, consistent with the theoretical value.

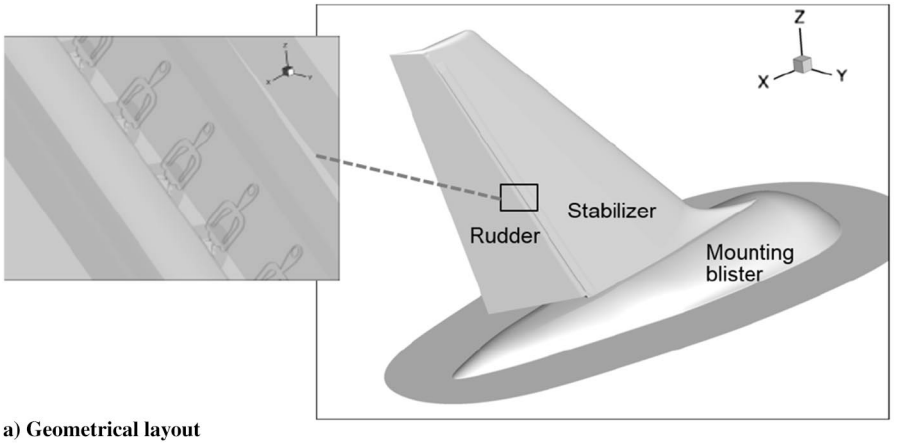

a) Geometrical layout

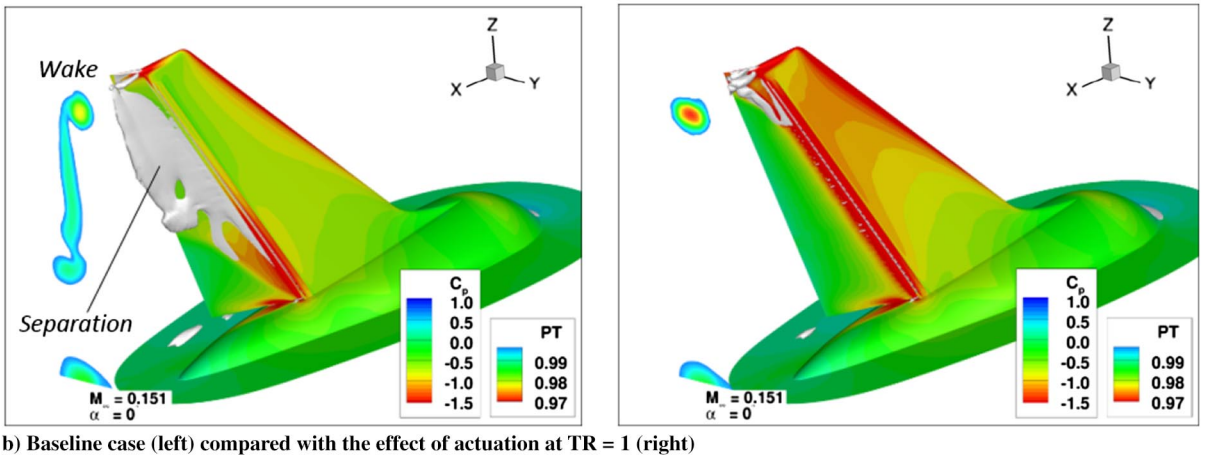

b) Baseline case (left) compared with the effect of actuation at TR = 1 (right)

Fig. 9 Thermal control application to the full-scale tail model with an array of fluidic oscillators.

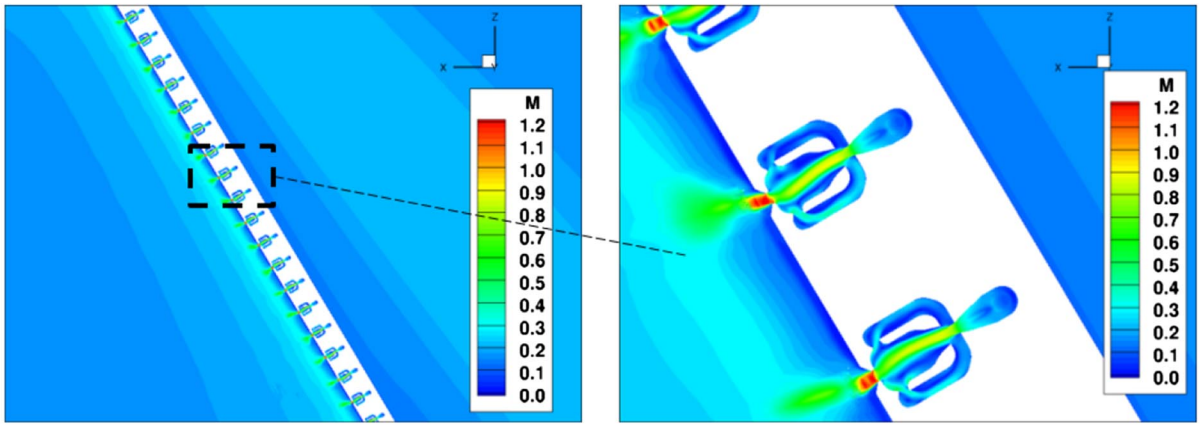

c) Cut through the actuator array showing instantaneous Mach number contours

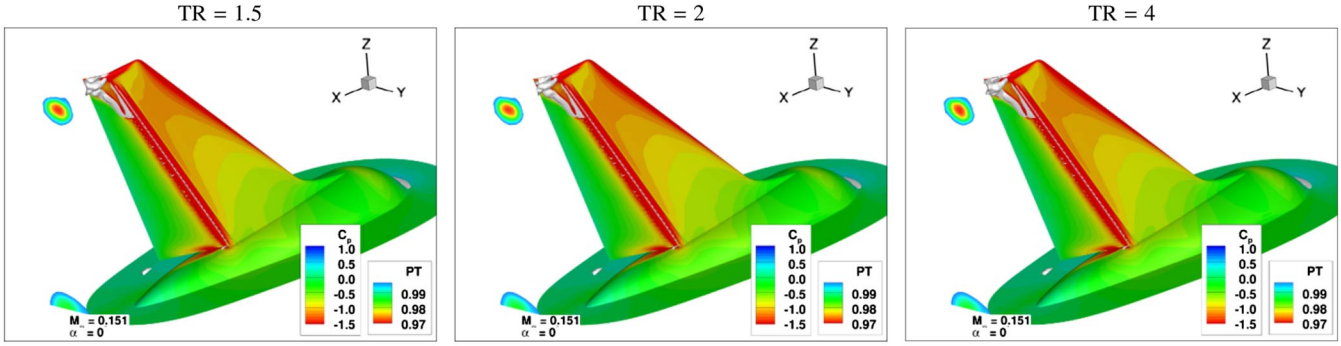

d) Effect of actuation at various TR

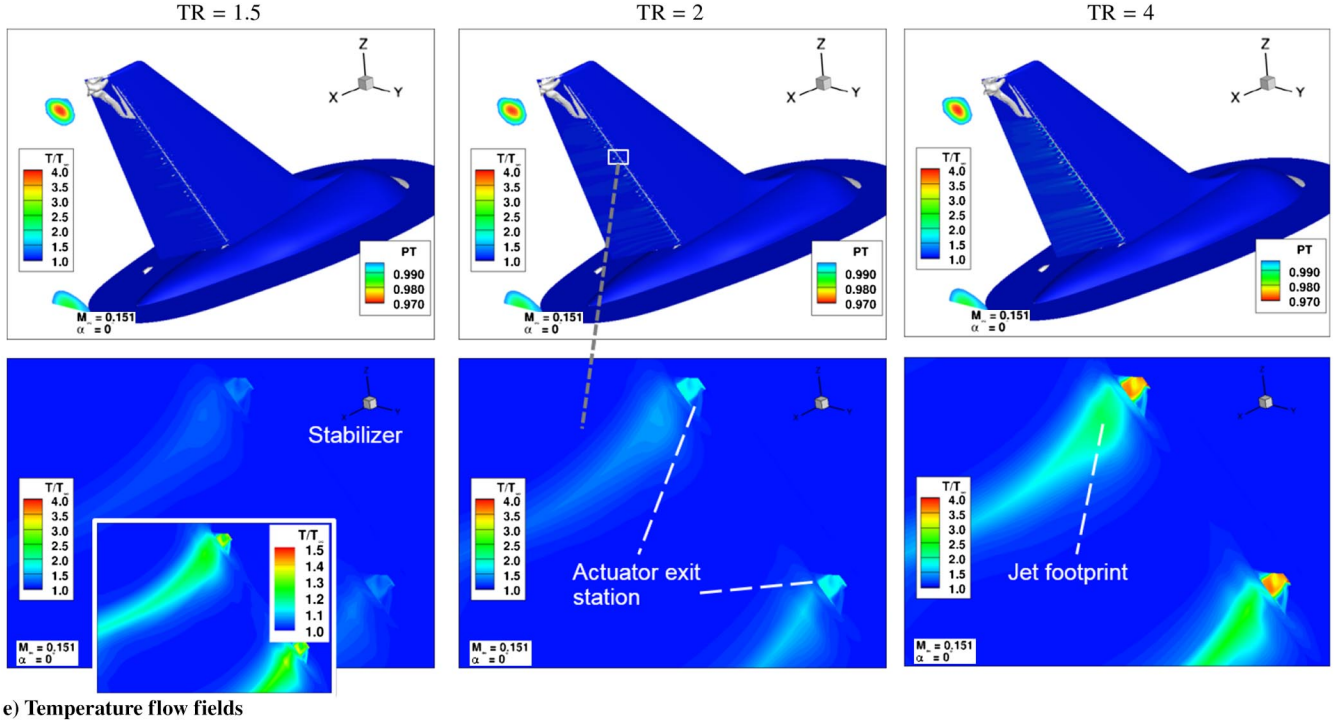

e) Temperature flow fields

Fig. 9 Continued.

B. High-Lift System

The thermal AFC method has been applied to a representative twin-engine, transonic long-range airplane for meeting performance requirements for takeoff and landing. The high-lift configuration shown in Fig. 11a consists of two span segments, simple-hinge flap system, the details of which are described in Refs. [9,34]. Although this configuration offers a set of advantages that potentially translates to significant airplane performance, its high-lift performance is unsatisfactory. Figure 11b shows the baseline flow (surface C_p and separation pattern) for a representative landing condition with the flaps deflected at 50 deg. The freestream Mach number is 0.2, and the angle of attack is 8 deg. The Reynolds number is 3.3 million based on the mean aerodynamic chord of the wing. These conditions result in flow separation that originates close to the hinge lines. This is especially evident on the inboard flap. The effect is less pronounced on the outboard flap due to the higher sweep. The flow separation in

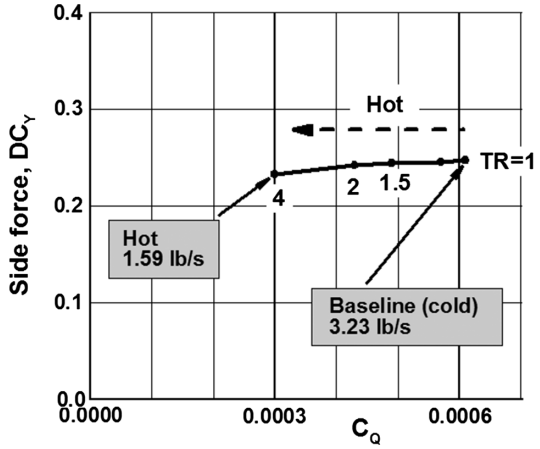

Fig. 10 Reduced mass flow rate due to thermal AFC on the vertical tail.

the aft portion of the wing results in reduced global circulation, commensurate with the rather low lift coefficient of $C_L = 1.4$.

The flow control system uses a very small continuous convergent–divergent nozzle spanning the length of the inboard flap segment. The nozzle throat height is 0.02% of the mean aerodynamic chord of the wing, and its area ratios are $A_{\text{th}}/A_{\text{in}} = 0.4$ and $A_{\text{th}}/A_{\text{ex}} = 0.6$. The diffuser is long enough to ensure that its half-angle is smaller than 15 deg to prevent the flow from separating. The exit section forms a long slot along the flap. The orifice of the nozzle is located just downstream of the flap hinge line, and it formed an approximate angle of 20 deg to the local flap surface. The results for PR = 6.4 and temperature ratios of TR = 1, 2, and 4 are shown in Figs. 11c and 11d. The black array of lines denotes the jet ejection vectors $\rho\bar{q}$ from the orifice.

The simulations indicate that, for all TR cases, the curtain of high-speed flow helps energize the viscous layer and prevents flow separation over the entire inboard flap element. Clearly, the temperature at the flap surface is elevated for the hot supply, although it dissipates quickly due to the mixing with the ambient stream. The flow properties at the midflap section in the vicinity of the nozzle show that the mass flow rate is reduced, but the momentum is nearly independent of the input temperature.

Figure 12 shows lift increments as a function of mass flow rate and momentum due to actuation. The point marked A denotes the baseline condition of $C_L = 1.4$. The black curves represent the cold input as actuation intensity varies with PR. A lift coefficient of $C_L \approx 1.9$ is achieved with PR = 6.4, resulting in $C_\mu = 0.0008$. This is equivalent to a 37% gain in lift relative to the nonactuated flow. Depending on supply temperature, the hot input helps lower the mass flow rate to the predicted levels, which are proportional to $T^{-(1/2)}$. However, it is noted that there is slight degradation in lift, especially for the TR = 4 case, where the lift gain is approximately 33%. Examination of the separation flow patterns indicates that there are inefficiencies of the flow control at high temperature at the inboard edge of the flap. Nevertheless, the thermal control is quite effective in reducing the required mass flow rate for a given level of lift, or equivalently, high-temperature/high-pressure supply attains higher lift levels for a given mass flow rate. These trends are observed even for lower actuation intensity, where the flow is partially separated, as indicated by the set of varying temperature cases with PR = 2.4. The collapse of the curves in the lift versus momentum plot reinforces the notion that the relevant parameter for AFC effectiveness is the momentum. Here, a given C_μ achieves the same lift level, independent of the flow properties of the air supply.

VI. Experimental Confirmations

A. Bench-Top Experiment with an Isolated Actuator

Experimental confirmation of the thermal AFC concept was first obtained on an actuator in a bench-top setting. The model illustrated in Fig. 13 was assembled from machined steel parts and high-temperature optical glass for optional schlieren access. The model includes high-temperature Kalrez O-rings, a heat shield to protect the temperature-sensitive force balance/load cell, and a high-temperature silicone RTV gasket material to bond the glass and the actuator plates. This assembly allows a maximum temperature of around 500 K (TR ≈ 1.68). The mass flow rate and air temperature were controlled by self-regulating controller units, an Omega FMA-2621A mass flow controller, and a Tutco-Farnam Cool Touch process air heater. The accuracy of the measurements was within 2% of the maximum value for the mass flow rate, within 1% for the pressure, and within 1% for the temperature. The convergent–divergent nozzle with $A_{\text{th}}/A_{\text{in}} = 0.4$ is similar to the geometry used in Sec. II. The only difference is the wider angle used for the experimental model (70 deg), which is not expected to have a material influence on the current thermal assessment. The nozzle has a depth of 0.1 in., a throat width of 0.2 in., and inlet width 0.5 in.

The effects of high-temperature supply were established through measurements of the mass flow coefficient C_Q, the momentum coefficient C_μ, and the pressure ratio PR. The pressure was measured with a pressure sensor. The coefficient C_Q was derived from the data acquired by the mass flow controller, and the momentum was approximated by force data obtained by a load cell. Because the temperature was controlled upstream of the setup, the temperature values at the inlet of the actuator were calculated using the pressure data to get a more accurate representation to account for heat losses between the controller and the actuator inlet. Based on this calculation procedure, the maximum value of the temperature ratio at the inlet of the actuator obtained in the course of this experiment was TR = 1.46.

The experimental data are summarized in Fig. 14, confirming the trends described in Sec. II. For the same pressure ratio, increasing the temperature ratio results in a reduced mass flow rate (Fig. 14a). However, the momentum C_μ is independent of the temperature ratio TR at the same PR (Fig. 14b). Both of these trends are captured in the C_μ versus C_Q plot (Fig. 14c), demonstrating that increased temperature ratio results in a reduced mass flow rate without affecting the momentum, or for a given C_Q, increasing both TR and PR results in higher C_μ.

In the next step, the mass flow coefficient C_Q is scaled by a factor of $1/\sqrt{\text{TR}}$. The results are summarized in Fig. 15, validating the analytical derivation of the thermal AFC concept.

B. Vertical-Tail Experiment

1. *Experimental Setup*

The final validation step was performed for a vertical tail, similar to the flow problem in Sec. IV.A. The vertical-tail model is tapered and swept back by $\Lambda = 42$ deg at the leading edge; it has a 35% chord rudder, a 0.538 m mean aerodynamic chord, and a span of 1.067 m; and it features a dorsal fin similar to what is used on a real stabilizer to smooth the transition between fuselage and stabilizer. Additional information can be found in Seele et al. [15]. For the implementation of the thermal actuation, the model was equipped with an array of 32 fluidic oscillators equally spaced (12.7 mm) along the hinge line at the trailing edge of the main element. The geometry of the actuators was identical and of the same size, with each actuator having a rectangular cross section of 0.04 by 0.08 in. at the throat. The actuators are embedded into the stabilizer upstream of the hinge line created by the deflected rudder and were machined into a compact array of planar actuator plates [35]. The flow ejection angle relative to the local surface was approximately 10 deg. The actuators were supplied with compressed air through a single point at the root of the model, thus creating a slight negative pressure gradient along the span. Hose forces were assessed in various different arrangements and found to exert negligible loads on the model (less than 1% of the smallest measured side force). The air supply was controlled, regulated, and recorded by an Omega FMA-2621A mass flow rate controller, and a Tutco Farnam Cool Touch process controller was used for the heat generation and regulation of the air temperature within a band of 2°C. The model is illustrated in Fig. 16b.

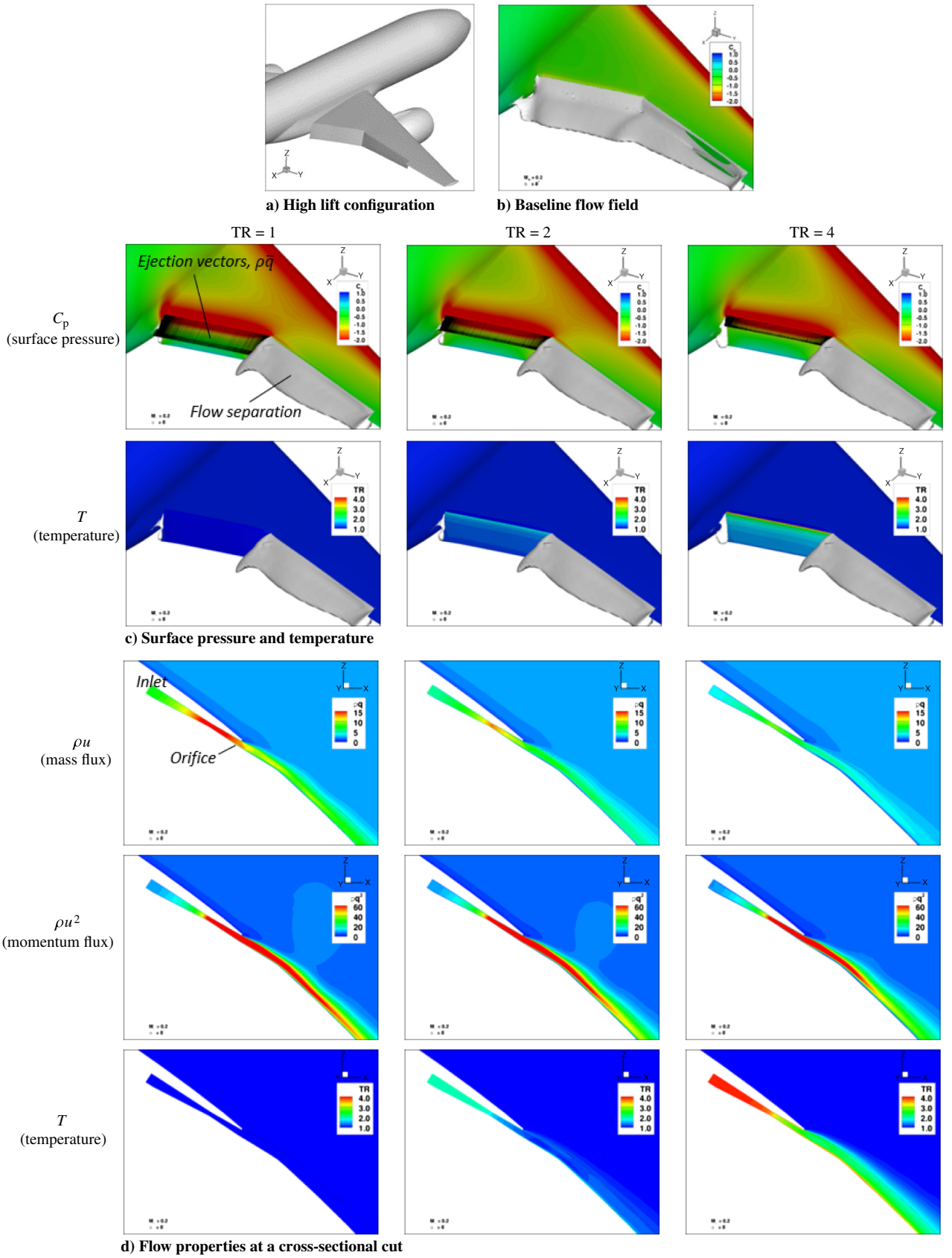

Fig. 11 Thermal control for the airplane high-lift system, PR = 6.4.

The tests were conducted in the California Institute of Technology's Lucas Wind Tunnel at a freestream velocity of 30 m/s with a rudder deflection of 10 deg. Figure 16 shows a schematic view of the vertical-tail model in the wind tunnel. The model is mounted on a rotating plate to allow testing at sideslip conditions. A fairing is installed to minimize interference effects of the viscous layer between the tunnel floor and the model root. The force balance, mass flow rate controller, and heat controller were

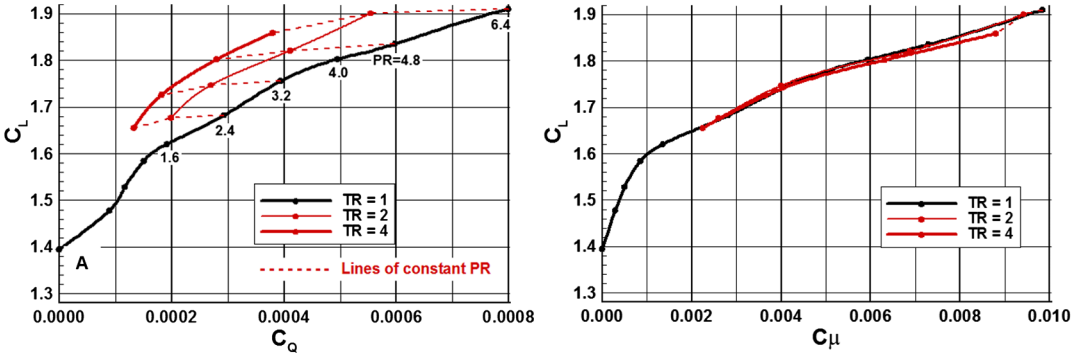

Fig. 12 Airplane performance due to thermal AFC at the nominal landing condition, $\alpha = 8$ deg.

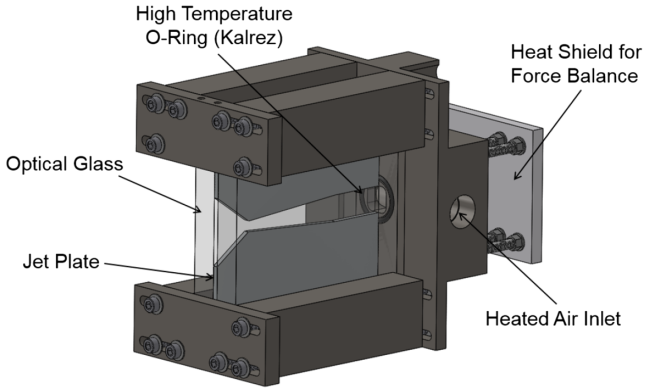

Fig. 13 Bench-top model of the convergent–divergent nozzle was designed to withstand high temperatures.

located below the test section of the wind tunnel. The rudder deflection was set to 20 deg for the results presented here.

2. *Effects of Thermal Active Flow Control*

To evaluate the effectiveness of thermal AFC, the side force of the vertical-tail model was measured for different mass flows rates and temperature ratios. Generally, the calculation of the momentum coefficient at the throat of the actuators presents a challenge in wind-tunnel experiments. A one-dimensional flow analysis was used to calculate C_μ based on C_Q, assuming an even distribution of the mass flow rate among the actuators. Similar to the bench-top setup, the temperature ratio was calculated based on the pressure inside the plenum at the actuator inlets.

Figure 17 shows the actuation parameters over the range of the temperature ratios for the vertical tail. Consistent with the previous results, for a given supply pressure, C_Q is reduced with increased

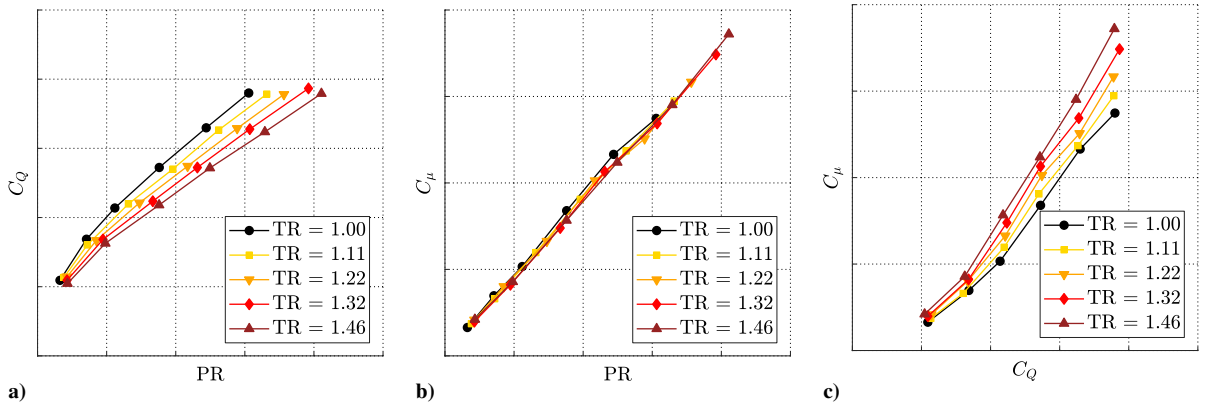

Fig. 14 Measurement results of the bench-top experiment.

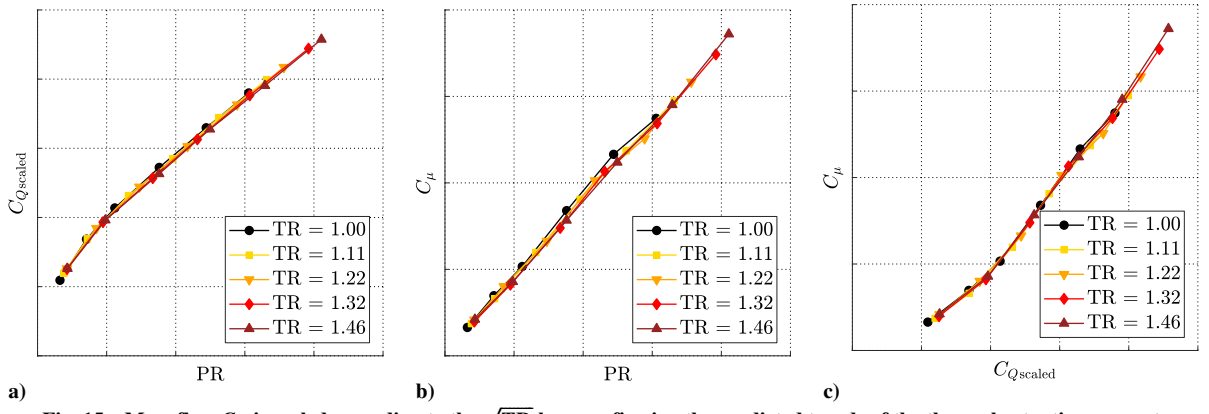

Fig. 15 Mass flow C_Q is scaled according to the $\sqrt{\text{TR}}$ law, confirming the predicted trends of the thermal actuation concept.

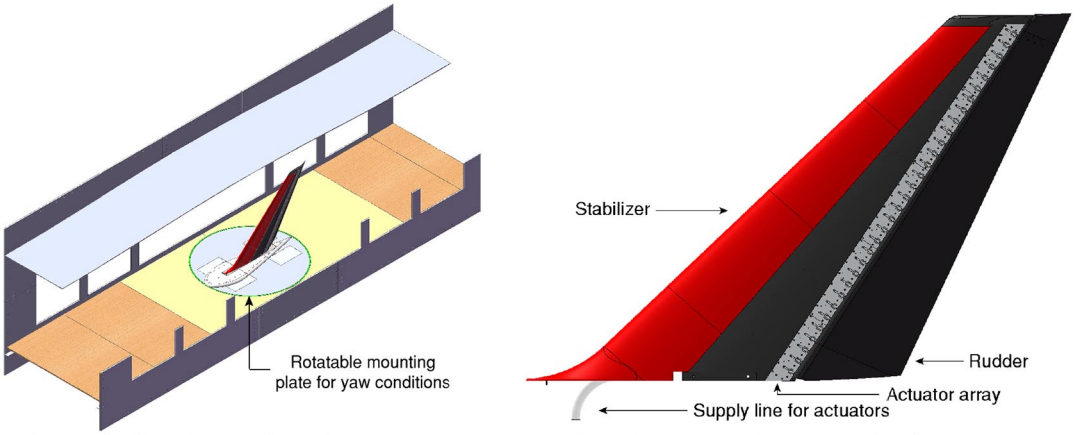

a) Schematic view of the vertical tail model mounted in the lucas wind tunnel

b) Vertical tail model seen from the suction side. The actuator covers were removed to expose the actuator array along the span

Fig. 16 Experimental setup of the vertical tail.

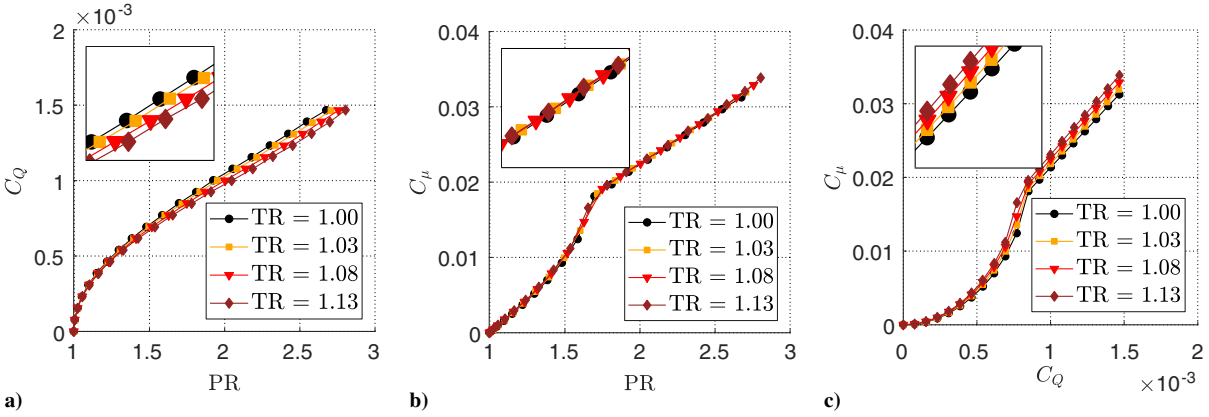

a) **b)** **c)**

Fig. 17 Influence of thermal AFC on the vertical tail.

temperature (Fig. 17a), essentially with no impact on C_μ (Fig. 17b). It can also be inferred from the C_μ versus C_Q plot (Fig. 17c) that, for the same mass flow rate, higher momentum is achieved by using an inflow with higher temperature and higher pressure, or using high supply temperature, the mass flow rate can be reduced to achieve the same C_μ.

Next, the actuation parameters are evaluated in Fig. 18 by scaling C_Q according to the $\sqrt{\text{TR}}$ law. The resulting plots clearly demonstrate that the predicted scaling factor is adequate for the characterization of thermal actuation.

Finally, the aerodynamic performance due to AFC is evaluated in Fig. 19. This is presented in terms of the incremental side-force coefficient C_Y' due to actuation relative to the baseline (AFC-off) case. This definition facilitates consistent evaluation and has the benefit of reducing small force balance offsets. For the same mass flow rate, the side force is increased with higher supply temperature (Fig. 19a). Equivalently, the same level of C_Y' is achieved with higher temperature, but with reduced C_Q. The applicability of the thermal concept for the side force is validated by scaling C_Q with $\sqrt{\text{TR}}$ (Fig. 19b). The side force is independent of the temperature ratio

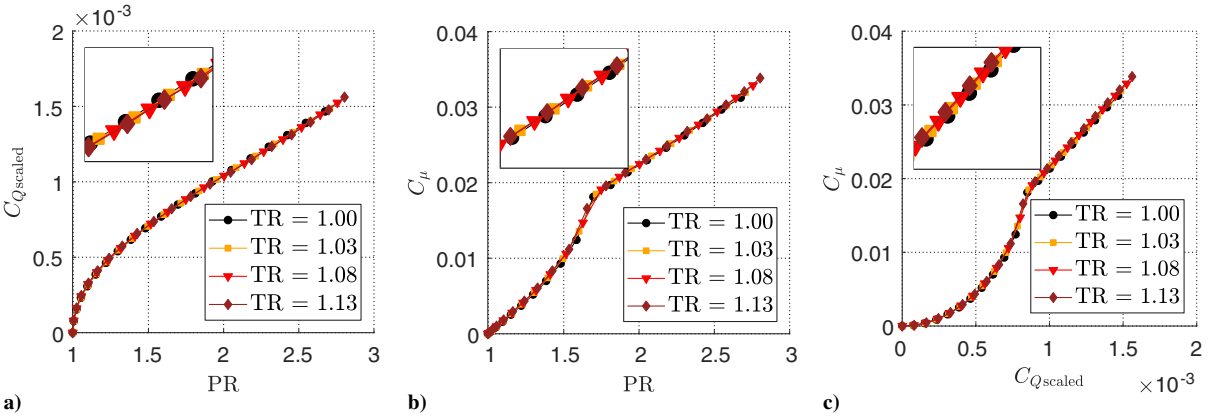

a) **b)** **c)**

Fig. 18 Mass flow C_Q scaled by the $\sqrt{\text{TR}}$ law causes a collapse of all the acquired data.

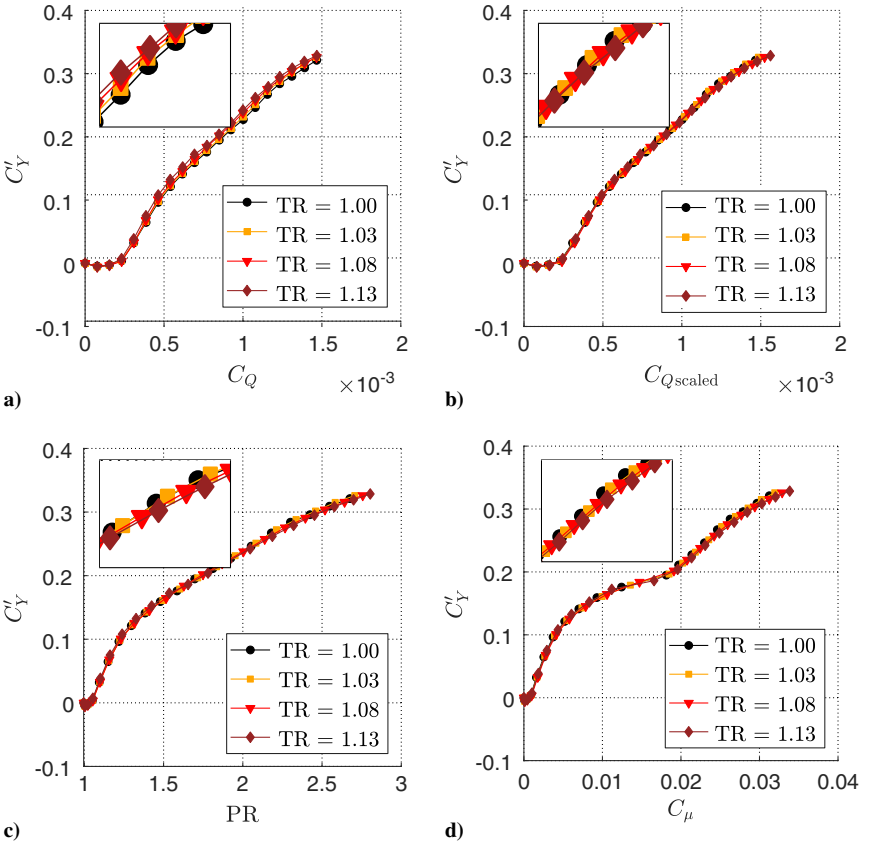

Fig. 19 Side-force effects due to thermal AFC.

(Fig. 19c), and compared with the momentum, it collapses for all temperature ratios (Fig. 19d). This confirms that an equivalent C_μ leads to the same side-force benefit, irrespective of the input flow properties. Similar to the high-lift application in Sec. V, these results demonstrate that C_μ is the relevant parameter for AFC effectiveness.

3. *Considerations for Future Testing*

Because the vertical-tail experiment used an existing model made of aluminum, an upper TR value of 1.13 was achieved for the evaluation of the thermal actuation. Excessive hot air was avoided to prevent structural damage to the plumbing system, including seals, glued connections, Teflon tape, and foam structures. Additionally, the aluminum structure of the vertical tail acted as a huge heat sink during the wind-tunnel runs. In fact, TR $= 1.37$ was supplied to the tail, but the air was cooled down to TR $= 1.13$ at the actuator inlet stations. Obviously, these practical limiting factors could be properly addressed had the model been built with the objective of high-temperature testing in mind. The challenges are mainly structural in nature and can be solved by using a material with certain properties: the ability to withstand high thermal stresses, with low heat-conductivity, yet able to carry the aerodynamic loads. A model made of ceramic material could be considered, but such material might be too brittle for wind-tunnel testing, and the cost of manufacturing might be prohibitive. The internal plumbing also needs to withstand high temperatures, possibly in combination with insulation blankets to avoid heat losses and protect nearby structures.

From an experimental point of view, achieving high TR levels is quite practical once the structural challenges are solved. The heater used in these experiments is able to reach values up to TR $= 2$ for fairly large mass flow rates (100 kg/h) and TR $= 3$ for moderate mass flow rates (30 kg/h), whereas the power consumption is well within a reasonable range (12.5 kW).

VII. Strategies for Thermal Flow Control Implementations

Although thermal AFC offers a low-input AFC solution, it presents a set of challenges for practical airframe integration. Clearly, in situations where high supply temperature is desired for use in conjunction with limited amount of mass flow, a special heating device is needed. The design of the heating device and power requirements are highly dependent on the particular application and the required input temperature (i.e., input mass flow rate). These challenges are addressed in the system integration design phase and are beyond the scope of the current paper.

The current approach introduces a new element in the design of AFC for future airplanes, whereby thermal actuation can be exploited for more efficient implementations. Fluidic actuation uses APU, engine bleed, or a compressor, which generally provide input at elevated temperatures relative to ambient conditions. It is common practice to use a heat exchanger to reduce the supply temperature to protect nearby structures. This was clearly illustrated during the ecoDemonstrator flight-test program, where a heat exchanger was installed in the aft fuselage to reduce the temperature of the supply from the APU, before reaching the AFC system. In situations when the supply is limited, a practical implementation might employ a higher supply temperature while designing the local structure to sustain higher thermal stresses. In essence, the thermal actuation approach provides another parameter for the designer of future AFC systems.

An optional system architecture that could take advantage of thermal control is in applications where the fluidic source is available at nominal temperature (i.e., cold supply). The plumbing system could be designed while considering nearby systems that operate at high temperature. The routing of pressurized air in a way that allows for heat transfer from high-temperature sources en route to the actuators might facilitate a low input AFC solution. One example is the upper-surface-blowing powered airplanes, which consist of engines mounted on the upper side of the wings. During high-lift operation, when the flaps are deployed, a portion of the engine exhaust plumes attach to the flap surfaces due to the Coanda effect, resulting in added lift production. This effect can be augmented by AFC at certain locations on the flap [12]. Here, the high-pressure air is provided by the engine fan. To lower the amount of bleed, the pressurized air could be routed to the flaps via regions adjacent to the

engine exhaust nozzle, where the high-temperature surroundings could be exploited to heat up the AFC fluid.

Finally, there are high-temperature flow processes where thermal AFC might be conveniently exploited (e.g., propulsion systems and combustion applications).

VIII. Conclusions

The objective of the current study was to develop a low-input actuation technique to address a key requirement in the design of integrated AFC systems for future flight platforms. This has led to the development of the thermal actuation technique, which is universally applicable to any type of fluidic actuation. The investigation presented here consists of the analytical derivation step, followed by computational assessments and experimental confirmations.

The actuation concept is derived from gas-dynamics principles, and it is based on thermal control of the air supply. It is shown that higher air supply temperature results in reduced mass flow rate with little or no degradation in AFC performance. Thermal actuation can also augment AFC effects for a given mass flow rate, by using a combined high-temperature/high-pressure supply. A computational method has been used to systematically investigate the hot air supply approach for blowing actuators and fluidic oscillators. The experimental confirmation of the thermal flow control concept was obtained for a constant blowing actuator in a bench-top setting.

The thermal control concept has been evaluated for airplane applications. The computational analyses include enhanced control authority of a vertical tail and improved performance of high-lift systems. Experimental validation was obtained for the vertical-tail model in a wind-tunnel setting. These airplane studies confirm the trends observed from the gas-dynamics analysis with respect to actuation mass flow rate as a function of supply temperature. Moreover, the temperature scaling parameter obtained from the analytical derivation is closely matched by both the computational predictions and the experimental measurements.

Strategies for the design of thermal actuation are presented. In applications where the supply is already at high temperature, it is advisable to consider designs that minimize temperature losses, thus enabling hot jet ejection for flow control. When the supply is at nominal temperature, a prudent design might use nearby subsystems that operate at high temperatures as heat sources.

Finally, an important outcome of the current investigation is the ability to establish the relevant parameter of AFC effectiveness for a specific application. Clearly, the momentum is the relevant parameter in the context of the separation control applications in this study. It is thereby recommended to use the supply temperature as a litmus test for establishing the proper AFC parameter for a specific application.

References

[1] Cattafesta, L., III, and Sheplak, M., "Actuators for Active Flow Control," *Annual Review of Fluid Mechanics*, Vol. 43, Jan. 2011, pp. 247–272. doi:10.1146/annurev-fluid-122109-160634

[2] Smith, B., and Glezer, A., "The Formation and Evolution of Synthetic Jets," *Physics of Fluids*, Vol. 10, No. 9, 1998, pp. 2281–2297. doi:10.1063/1.869828

[3] Glezer, A., and Amitay, M., "Synthetic Jets," *Annual Review of Fluid Mechanics*, Vol. 34, 2002, pp. 503–529. doi:10.1146/annurev.fluid.34.090501.094913

[4] Margalit, S., Greenblatt, D., Seifert, A., and Wygnanski, I., "Delta Wing Stall and Roll Control Using Segmented Piezoelectric Fluidic Actuators," *Journal of Aircraft*, Vol. 42, No. 3, 2005, pp. 698–709. doi:10.2514/1.6904

[5] Melton, L. P., Hannon, J., Yao, C.-S., and Harris, J., "Active Flow Control at Low Reynolds Numbers on a NACA 0015 Airfoil," *26th AIAA Applied Aerodynamics Conference*, AIAA Paper 2008-6407, Aug. 2008. doi:10.2514/6.2008-6407

[6] Rathay, N., Boucher, M., Amitay, M., and Whalen, E., "Performance Enhancement of a Vertical Tail Using Synthetic Jet Actuators," *AIAA Journal*, Vol. 52, No. 4, 2014, pp. 810–820. doi:10.2514/1.J052645

[7] Milholen, W., Jones, G., Chan, D., Goodliff, S., Anders, S., Melton, L., Carter, M., Allan, B., and Capone, F., "Enhancements to the FAST-MAC Circulation Control Model and Recent High-Reynolds Number Testing in the National Transonic Facility," *31st AIAA Applied Aerodynamics Conference*, AIAA Paper 2013-2794, 2013. doi:10.2514/6.2013-2794

[8] Müller-Vahl, H., Strangfeld, C., Nayeri, C., Paschereit, C., and Greenblatt, D., "Control of Thick Airfoil, Deep Dynamic Stall Using Steady Blowing," *AIAA Journal*, Vol. 53, No. 2, 2014, pp. 277–295. doi:10.2514/1.J053090

[9] Shmilovich, A., Yadlin, Y., Dickey, E., Hartwich, P., and Khodadoust, A., "Development of an Active Flow Control Technique for an Airplane High-Lift Configuration," *55th AIAA Aerospace Sciences Meeting*, AIAA Paper 2017-0322, 2017. doi:10.2514/6.2017-0322

[10] Shmilovich, A., and Yadlin, Y., "Engine Vortex Flows and Methods of Ground Vortex Alleviation," *Proceedings of the 3rd International Conference on Vortex Flows and Vortex Models (ICVFM2005)*, Yokohama, Japan, 2005, pp. 21–26.

[11] Ciobaca, V., Rudnik, R., Haucke, F., and Nitche, W., "Active Flow Control on a High-Lift Airfoil: URANS Simulations and Comparison with Time-Accurate Measurements," *31st AIAA Applied Aerodynamics Conference*, AIAA Paper 2013-2795, 2013. doi:10.2514/6.2013-2795

[12] Yadlin, Y., and Shmilovich, A., "Lift Enhancement for Upper Surface Blowing Airplanes," *31st AIAA Applied Aerodynamics Conference*, AIAA Paper 2013-2796, 2013. doi:10.2514/6.2013-2796

[13] Meyer, M., Machunze, W., and Bauer, M., "Towards the Industrial Application of Active Flow Control in Civil Aircraft—An Active Highlift Flap," *32nd AIAA Applied Aerodynamics Conference*, AIAA Paper 2014-2401, 2014. doi:10.2514/6.2014-2401

[14] Bauer, M., Grund, T., and Nitsche, W., "Experiments on Active Drag Reduction on a Complex Outer Wing Model," *AIAA Journal*, Vol. 53, No. 7, 2014, pp. 1774–1783. doi:10.2514/1.J053515

[15] Seele, R., Graff, E., Lin, J., and Wygnanski, I., "Performance Enhancement of a Vertical Tail Model with Sweeping Jet Actuators," *51st AIAA Aerospace Sciences Meeting*, AIAA Paper 2013-0411, Jan. 2013. doi:10.2514/6.2013-411

[16] Vatsa, V., Casalino, D., Lin, J., and Appelbaum, J., "Numerical Simulation of a High-Lift Configuration with Embedded Fluidic Actuators," *32nd AIAA Applied Aerodynamics Conference*, AIAA Paper 2014-2142, 2014. doi:10.2514/6.2014-2142

[17] Whalen, E. A., Lacy, D. S., Lin, J. C., Andino, M. Y., Washburn, A. E., Graff, E. C., and Wygnanski, I. J., "Performance Enhancement of a Full-Scale Vertical Tail Model Equipped with Active Flow Control," *53rd AIAA Aerospace Sciences Meeting*, AIAA Paper 2015-0784, 2015. doi:10.2514/6.2015-0784

[18] Shmilovich, A., Yadlin, Y., and Whalen, E. A., "Numerical Simulations of an Airplane with an Active Flow Control System," *8th AIAA Flow Control Conference*, AIAA Paper 2016-3929, 2016. doi:10.2514/6.2016-3929

[19] Yadlin, Y., and Shmilovich, A., "Computational Method for Assessment of Flow Control Techniques for Airplane Propulsion Systems," *4th Flow Control Conference*, AIAA Paper 2008-4084, June 2008. doi:10.2514/6.2008-4084

[20] Shmilovich, A., and Yadlin, Y., "Flow Control of Airplane Tailing Wakes," *Proceedings of the 4th International Conference on Vortex Flows and Models (ICVFM2008)*, Daejeon, Republic of Korea, 2008, pp. 132–141.

[21] Shmilovich, A., and Yadlin, Y., "Flow Control Techniques for Transport Aircraft," *AIAA Journal*, Vol. 49, No. 3, 2011, pp. 489–502. doi:10.2514/1.J050400

[22] Shmilovich, A., and Yadlin, Y., "Traverse Actuation Method," *8th AIAA Flow Control Conference*, AIAA Paper 2016-3309, 2016. doi:10.2514/6.2016-3309

[23] Crittenden, T., Glezer, A., Funk, R., and Parekh, D., "Combustion-Driven Jet Actuators for Flow Control," *15th AIAA Computational Fluid Dynamics Conference*, AIAA Paper 2001-2768, 2001. doi:10.2514/6.2001-2768

[24] Crittenden, T., and Raghu, S., "Combustion Powered Actuator with Integrated High Frequency Oscillator," *International Journal of Flow Control*, Vol. 1, No. 1, 2009, pp. 87–97. doi:10.1260%2F1756-8250.1.1.87

[25] Andino, M., Lin, J., Washburn, A., Whalen, E., Graff, E., and Wygnanski, I., "Flow Separation Control on a Full-Scale Vertical Tail Model Using Sweeping Jet Actuators," *53rd AIAA Aerospace Sciences Meeting*, AIAA Paper 2015-0785, 2015. doi:10.2514/6.2015-0785

[26] Whalen, E., Shmilovich, A., Spoor, M., Tran, J., Vijgen, P., Lin, J. C., and Andino, M., "Full-Scale Flight Demonstration of an Active Flow Control Enhanced Vertical Tail," *8th AIAA Flow Control Conference*, AIAA Paper 2016-3927, 2016.
doi:10.2514/6.2016-3927

[27] Shmilovich, A., and Whalen, E., "A Technique for Low Input Flow Control Actuation," *35th AIAA Applied Aerodynamics Conference*, AIAA Paper 2017-3040, 2017.
doi:10.2514/6.2017-3040

[28] Buning, P., Chiu, I.-T., Obayashi, S., Rizk, Y., and Steger, J., "Numerical Simulation of the Integrated Space Shuttle Vehicle in Ascent," *15th Atmospheric Flight Mechanics Conference*, AIAA Paper 1988-4359, 1988.
doi:10.2514/6.1988-4359

[29] Shmilovich, A., and Yadlin, Y., "Flow Control for the Systematic Buildup of High-Lift Systems," *Journal of Aircraft*, Vol. 45, No. 5, 2008, pp. 1680–1688.
doi:10.2514/1.35327

[30] Shmilovich, A., and Yadlin, Y., "Active Flow Control for Practical High-Lift Systems," *Journal of Aircraft*, Vol. 46, No. 4, 2009, pp. 1354–1364.
doi:10.2514/1.41236

[31] Shmilovich, A., Yadlin, Y., and Whalen, E., "Computational Evaluation of Flow Control for Enhanced Control Authority of a Vertical Tail," *AIAA Journal*, Vol. 54, No. 8, 2016, pp. 2211–2220.
doi:10.2514/1.J054712

[32] Khodadoust, A., and Shmilovich, A., "High Reynolds Number Simulations of Distributed Active Flow Control for a High-Lift System," AIAA Paper 2007-4423, 2007.
doi:10.2514/6.2007-4423

[33] Seele, R., Graff, E., Gharib, M., Taubert, L., Lin, J., and Wygnanski, I., "Improving Rudder Effectiveness with Sweeping Jet Actuators," *6th AIAA Flow Control Conference*, AIAA Paper 2012-3244, June 2012.
doi:10.2514/6.2012-3244

[34] Hartwich, P., Shmilovich, A., Lacy, D., Dickey, E., Sclafani, A., Sundaram, P., and Yadlin, Y., "Refined AFC-Enabled High-Lift System Integration Study," NASA CR-2016-219170, 2016.

[35] Raghu, S., "Method and Apparatus for Aerodynamic Flow Control Using Compact High-Frequency Fluidic Actuator Arrays," U.S. Patent 8,382,043, Feb. 2013.

D. Greenblatt
Associate Editor